NASA Technical Memorandum 106772

A Modified Mixing Length Turbulence Model for Zero and Adverse Pressure Gradients

J.M. Conley
Lewis Research Center
Cleveland, Ohio

and

B.P. Leonard
The University of Akron
Akron, Ohio

Prepared for the
30th Joint Propulsion Conference
cosponsored by AIAA, ASME, SAE, and ASEE
Indianapolis, Indiana, June 27–29, 1994

National Aeronautics and
Space Administration

A MODIFIED MIXING LENGTH TURBULENCE MODEL FOR ZERO AND ADVERSE PRESSURE GRADIENTS

J.M. Conley
National Aeronautics and Space Administration
Lewis Research Center
Cleveland, Ohio 44135

and

B.P. Leonard
The University of Akron
Akron, Ohio 44325

Abstract

The modified mixing length (MML) turbulence model was installed in the Proteus Navier-Stokes code, then modified to make it applicable to a wider range of flows typical of aerospace propulsion applications. The modifications are based on experimental data for three flat-plate flows having zero, mild adverse, and strong adverse pressure gradients. Three transonic diffuser test cases were run with the new version of the model in order to evaluate its performance. All results are compared with experimental data and show improvements over calculations made using the Baldwin-Lomax turbulence model, the standard algebraic model in Proteus.

Nomenclature

A^+	van Driest damping constant = 26
c_f	local skin friction coefficient
C_l	MML parameter; controls mixing length saturation level
C_2	MML parameter; controls curvature of blending region
C_{cp}	Baldwin-Lomax turbulence model constant = 1.6
C_{Kleb}	Baldwin-Lomax turbulence model constant = 0.3
C_{wk}	Baldwin-Lomax turbulence model constant = 0.25
D_1, D_2	parameters used in turbulence model averaging for multiple walls
f_1, f_2	parameters used in turbulence model averaging for multiple walls
F(y)	function in Baldwin-Lomax turbulence model
F_{Kleb}	Klebanoff intermittency factor
F_{max}	parameter in Baldwin-Lomax turbulence model
F_{wake}	parameter in Baldwin-Lomax turbulence model
G_1,...G_8	MMLPG parameters
H	throat height of Sajben diffuser
k	coefficient of thermal conductivity
l	turbulent mixing length
p	static pressure
p_t	total pressure
Q	vector of dependent variables
R	ratio of exit static pressure to inlet total pressure for Sajben diffuser
Re_x	Reynolds number based on x-coordinate
t	time
u, v	velocities
u_∞	freestream x-velocity
u_τ	shear velocity
V	total velocity
V_{diff}	difference between maximum and minimum total velocities
x, y	Cartesian coordinates
y^+	y coordinate nondimensionalized by shear length scale
y^*	shear length scale
y_{max}	parameter in Baldwin-Lomax turbulence model
β	Clauser's equilibrium parameter
δ	boundary layer thickness
δ_1	displacement thickness
$\varepsilon_E^{(2)}$, $\varepsilon_E^{(4)}$	second- and fourth-order artificial viscosity coefficients in constant coefficient model
ε_I	implicit artificial viscosity coefficient
κ	von Karman constant = 0.4
κ_2, κ_4	constants in nonlinear coefficient artificial viscosity model
λ	second coefficient of viscosity
μ	molecular viscosity
ξ, η	computational coordinate directions
ρ	density

* Aerospace Engineer, Member AIAA
† Professor of Mechanical Engineering, Member AIAA

σ	pressure gradient scaling parameter in nonlinear coefficient artificial viscosity model
ψ	spectral radius in nonlinear coefficient artificial viscosity model
τ	shear stress
τ_1, τ_2	shear stress at interior grid points
ω	vorticity

Subscripts

cap	capping or saturation value
e	edge of boundary layer
eff	effective
i, j	indexes in the x and y directions
inner	inner region of boundary layer
max	maximum
min	minimum
outer	outer region of boundary layer
t	turbulent
w	wall

Superscripts

+	nondimensionalized by the shear length scale

Introduction

The Proteus Navier-Stokes code[1] was developed for aerospace propulsion flow applications and solves the Reynolds-averaged, unsteady, compressible Navier-Stokes equations in strong conservation-law form. It uses a fully-coupled alternating direction implicit solution procedure[2] with generalized first or second order time differencing,[3] employs implicit boundary conditions, and linearizes all terms using second order Taylor series expansions. Two turbulence models are available in Proteus: The Baldwin-Lomax algebraic model (BLM)[4] and the Chien k-ε model.[5]

For engineering applications, algebraic models offer the most algorithmically simple and computationally efficient approach to turbulence modeling. Though two-equation models are sometimes thought to be more accurate at calculating complex flows, they are more difficult to implement, require initial and boundary conditions that are often difficult to define, and are usually more computationally expensive than algebraic models. The Baldwin-Lomax model (presented in Appendix A) is the most widely used algebraic model, even though it is known to have difficulties computing flows with strong adverse pressure gradients and large separated regions.[6-14] The modified mixing length model (MML) was developed specifically to handle the separation that occurs on airfoils with leading edge ice accretions, and it produced significantly better results than BLM for such flows.[6] The success of these calculations warrants further evaluation and development of MML.

The objective of this work is to evaluate and then modify MML to improve its performance for adverse pressure gradient flows. To accomplish this, MML was installed in Proteus and first used to calculate zero pressure gradient flow over a flat plate. It was modified to more accurately predict the boundary layer growth for this flow; then the experimental data of Bradshaw[15] was used to make additional modifications for adverse pressure gradient flows. The resulting model, called MMLPG, was then validated for three transonic diffuser test cases. The CRAY Y-MP computer at the NASA Lewis Research Center was used for all calculations.

The MML Model

The modified mixing length model was developed by Potapczuk[6] to fill the need for an algebraic model to calculate turbulent flow with large separated regions. The particular problem of interest was an airfoil at angle of attack with and without leading edge ice accretions. Previous calculations made with BLM produced nonphysical results; the source of the problem was the function F(y) (defined in Appendix A), which could have multiple peaks for this flow. This behavior is shown in figure 1, taken from reference 6. As the relative magnitudes of the F(y) local maxima change, y_{max} may suddenly jump, producing unrealistic discontinuities in the turbulent viscosity. Selection of the global maxima often results in a gross over-prediction of the turbulent viscosity. Some authors[8, 9] have found that choosing the outermost peak produces better results, while others have elected to use the innermost peak.[10]

The MML model avoids the need to seek a maximum of some ad hoc function. In accordance with Prandtl's mixing length theory, the MML model determines the mixing length using the wall shear stress and the normal distance from the wall, with the maximum mixing length capped at a given value. As a result, it is a two layer model; the length scale depends on conditions near the surface and remains constant in the separated region. This assumption is valid since there is no substantial enhancement of turbulence in separated regions. The turbulent viscosity, μ_t, is given by

$$\mu_t = \rho l^2 |\omega| \tag{1}$$

where ρ is the density, l is the mixing length and $|\omega|$ is the vorticity magnitude. Figure 2, taken from reference 16, shows the behavior of the mixing length in a turbulent boundary layer. Several empirical formulas are available to evaluate the inner region,[16, 17] which

consists of the viscous sublayer and the overlap layer. The MML model uses the van Driest formulation,[16] given by

$$l_{inner} = \kappa y\left(1 - e^{-\frac{y^+}{A^+}}\right) \quad (2)$$

where $A^+ = 26$ and the value of κ, the von Karman constant, is 0.4. The quantity y^+ is defined as

$$y^+ = \frac{y}{y^*} \quad (3)$$

where y^* is the shear length scale

$$y^* = \frac{\mu}{\sqrt{\rho|\tau_w|}} \quad (4)$$

Here, μ is the molecular viscosity and τ_w is the wall shear stress. For $y^+ \geq 5A^+$ (but still in the "inner" region), the mixing length is approximated by κy; this is the original Prandtl theory, and is consistent with the well-known logarithmic profile. In the outer region of the boundary layer, the outer mixing length is assumed to behave according to

$$l_{outer} = \text{constant} \times y^* \quad (5)$$

The MML model uses a blending function to give a smooth transition between the inner and outer layers; this is given by

$$l(y) = \kappa\frac{C_1}{C_2}y^*\left(1 - \left(1 - \frac{y^+}{C_1}\right)^{C_2}\right)\left(1 - e^{-\frac{y^+}{A^+}}\right), \quad y^+ < C_1 \quad (6)$$

$$l(y) = \kappa\frac{C_1}{C_2}y^*, \quad y^+ \geq C_1 \quad (7)$$

In this formulation, $C_1 y^*$ is the distance from the surface at which l saturates, and C_2 controls the curvature of the blending region. Figure 3 shows a typical MML model mixing length profile for an attached wall boundary layer.

Near separated regions, τ_w approaches zero which causes y^* and thus the mixing length to become very large. To avoid this problem, the following local average was incorporated:[6]

$$|\tau_i| = 0.1|\tau_{i-2}| + 0.2|\tau_{i-1}| + 0.4|\tau_i| + 0.2|\tau_{i+1}| + 0.1|\tau_{i+2}| \quad (8)$$

The subscripts in equation (8) refer to grid points in the streamwise direction along the wall.

Calculations for iced airfoil flows made by Potapczuk with the MML model showed improvements over BLM calculations for predictions of the separated region, the maximum lift coefficient and vortex shedding frequencies. Since the MML model was developed to solve the specific problem of flow over airfoils, a comprehensive evaluation of the model for more general flow fields was not a part of that study. The objective of the present study is to evaluate the MML model for general zero pressure gradient and adverse pressure gradient turbulent boundary layer flows and examine possible modifications to improve the performance of the model.

Evaluation and Modification of MML

Evaluation of MML for Zero Pressure Gradient Flow

The test case of incompressible, zero pressure gradient, turbulent flow over a flat plate, as shown in figure 4, was used to evaluate MML. The grid, shown in figure 5, had 51 points in both the streamwise and normal directions and had grid points clustered at the wall to resolve the boundary layer and at the upstream boundary to resolve the imposed boundary condition. In addition, it was evaluated to insure grid independence for zero pressure gradient flow. The reference velocity, temperature, pressure and length used in Proteus were 33.53 m/s, 288.3 K, 101.3 kPa and 1.98 m, respectively. At the upstream boundary, the velocity profile, which was computed using the correlation of Musker,[18] was held fixed. The flow was computed using both MML and BLM. The MML constants were chosen as C_1=3000 and C_2=5, which were found to give good results at Re_x=7x10^6. Both turbulence models produced good agreement with experimental velocity-defect profiles,[19] as shown in figure 6 at Re_x=7x10^6. The quantity u_τ in figure 6 is the shear velocity, given by $u_\tau = \sqrt{(|\tau_w|/\rho)}$. At other locations on the plate (i.e., at other Reynolds numbers) the BLM velocity-defect profiles correctly exhibit similarity but the MML profiles do not, as shown in figure 7.

In a turbulent flow over a flat plate, the boundary layer thickness increases with increasing x-distance along the plate. To accurately model this flow, the turbulent length scale must also increase proportionately with

the boundary layer thickness. In MML, the outer length scale, as given in equation (7) is equal to a constant times the shear length scale, y^*. The increase in y^* with x-distance is almost negligible, resulting in an essentially constant value of the outer length scale for all Reynolds numbers. Plots of μ_t, as shown in figure 8, illustrate that the turbulent viscosity profiles calculated with MML are nearly the same at all Reynolds numbers, but the BLM μ_t profiles increase with increasing Reynolds number. Though MML produced the correct length scales for an airfoil near stall,[6] modifications are needed to make it applicable to general boundary layer flows.

In order to make MML applicable over a range of Reynolds numbers, the optimal saturation lengths, or C_l values, were found at several Reynolds numbers. The following simplified formulas were used to calculate the inner and outer mixing lengths:

$$l^+ = \kappa y^+ \left(1 - e^{-\frac{y^+}{A^+}}\right), \qquad C_l < y^+ \tag{9}$$

$$l^+_{cap} = \kappa C_l, \qquad C_l \geq y^+ \tag{10}$$

Here, l^+ is the nondimensional form of the mixing length, equivalent to l/y^*, and the outer length scale, l^+_{cap}, is simply the inner length scale evaluated at $y^+ = C_l$. From these results, l^+_{cap} was found as a function of the skin friction, c_f, giving

$$l^+_{cap} = 1860 - 6.20 \times 10^5 c_f \tag{11}$$

The velocity-defect profiles of figure 9 show that equations (9) and (11) with $l^+ = \min(l^+, l^+_{cap})$, allow the mixing length to grow proportionately with the boundary layer thickness. The modified MML is better than BLM at predicting the local skin friction coefficient, c_f, as shown in figure 10; the wiggles at the upstream boundary are a result of the imposed upstream boundary condition.

Modifications for Adverse Pressure Gradient Flows

Two equilibrium pressure gradient flows of Bradshaw[15] were used to modify MML for adverse pressure gradients effects. Equilibrium turbulent flows are flows which have a constant value of Clauser's equilibrium parameter,[21]

$$\beta = \frac{\delta_1}{\tau_w}\frac{\partial p_e}{\partial x} \tag{12}$$

In addition, they correspond to a power-law velocity profile distribution, $u_e \propto x^a$, where the magnitude of the exponent, a, indicates the strength of the pressure gradient. They also exhibit similarity when plotted in velocity-defect coordinates. Three flows were examined in the experimental study of Bradshaw;[15] these were flows with zero, mild, and strong adverse pressure gradients. The corresponding values of the exponent, a, are 0, -0.15, and -0.255, respectively; the corresponding values of β are 0, 1 and 5.

The modifications to the turbulence model are based on the trends exhibited in the mixing length at the three pressure gradients as shown in figure 11 taken from Bradshaw.[15] Note that for all three pressure gradients, the maximum mixing length is approximately 0.08δ, the saturation distance from the wall is approximately 0.4δ, and the slope of the curves near the wall increases with the strength of the pressure gradient. These three features were used to develop the following model:

$$l^+ = \kappa G_3 \frac{G_1}{G_2}\left(1 - \left(1 - \frac{y^+}{G_1}\right)^{G_2}\right)\left(1 - e^{-\frac{y^+}{A^+}}\right), \qquad y^+ < G_1 \tag{13}$$

$$l^+ = \kappa G_3 \frac{G_1}{G_2}, \qquad y^+ > G_1 \tag{14}$$

A new parameter, G_3, has been introduced and the constants C_1 and C_2 in the original MML model have been replaced by the functions G_1 and G_2, where

$$G_1 = 0.4 G_4 \tag{15}$$

$$G_2 = 5 G_3 \kappa \tag{16}$$

Here, G_4 is essentially a nondimensional boundary layer thickness which is a function of β and c_f, and G_3 controls the slope of the mixing length curve and is a function of β. The following correlation was assumed for G_4:

$$G_4 = G_5 + G_6 c_f \tag{17}$$

Separate values of the parameters G_3, G_5, and G_6, corresponding to each of the three pressure gradients, were found and are given in table 1. This results in essentially three separate models, one for each pressure gradient, depending on the set of parameters used. The results of

these modifications are compared with Baldwin-Lomax calculations in the velocity-defect plots of figures 12 through 14. (Note: The Baldwin-Lomax results for the zero pressure gradient case are given in figure 7.) The reference conditions used are the same as those given earlier for the zero pressure gradient case. For the two adverse pressure gradient cases, the turbulent velocity profiles at the upstream boundary were computed using a cubic spline fit of the Bradshaw experimental data and held fixed; the appropriate pressure gradient was imposed at the freestream boundary. Both cases were computed using the grid of figure 5, but for the strong pressure gradient case, the number of grid points in the vertical direction was increased to 101.

Final Model

The final step in developing this turbulence model was to combine all of the above modifications into one general turbulence model. To accomplish this, the following correlations were developed for the parameters G_3, G_5 and G_6:

$$G_3 = 1.0 \qquad \beta < 0.0 \tag{18.a}$$

$$G_3 = 1.0 + 0.307\beta - 0.0391\beta^2 \qquad 0.0 \le \beta \le 5.34 \tag{18.b}$$

$$G_3 = 1.52 \qquad \beta > 5.34 \tag{18.c}$$

$$G_5 = 23,300 \qquad \beta < 0.0 \tag{18.d}$$

$$G_5 = 23,300 + 8560\beta - 1230\beta^2 \qquad 0.0 \le \beta \le 5.34 \tag{18.e}$$

$$G_5 = 33,900 \qquad \beta > 5.34 \tag{18.f}$$

$$G_6 = -7.75 \times 10^6 \qquad \beta < 0.0 \tag{18.g}$$

$$G_6 = -7.75 \times 10^6 - 4.51 \times 10^6\beta + 386,000\beta^2 \qquad 0.0 \le \beta \le 5.34 \tag{18.h}$$

$$G_6 = -20,900 \qquad \beta > 5.34 \tag{18.i}$$

The available experimental data are limited to only the three values of β which are in the range $0 \le \beta \le 5.34$, and the quadratic correlations of equations (18.b), (18.e) and (18.h) are based on this limited data. For $\beta<0$, the values in (18.a), (18.d) and (18.g), were obtained by evaluating the quadratic equations at $\beta=0$. Similarly, for $\beta>5.34$, the values in (18.c), (18.f) and (18.i) were obtained by evaluating the quadratic equations at $\beta=5.34$.

Since β, defined in equation (12), is a function of the displacement thickness, δ_1, a correlation was also developed to avoid the problem of calculating δ_1 directly and thus having to define the edge of the boundary layer. This resulted in

$$\delta_1 = (G_7 + G_8 c_f)\, y^* \tag{19}$$

The parameters G_7 and G_8 were defined in a manner similar to G_3, G_5 and G_6 as given below.

$$G_7 = 2910 \qquad \beta < 0 \tag{20.a}$$

$$G_7 = 2910 + 2700\beta - 343\beta^2 \qquad 0 \le \beta \le 5.34 \tag{20.b}$$

$$G_7 = 7560 \qquad \beta \ge 5.34 \tag{20.c}$$

$$G_8 = -96900 \qquad \beta < 0 \tag{20.d}$$

$$G_8 = -988,000 - 1.15 \times 10^6\beta + 89,000\beta^2 \qquad 0 \le \beta \le 5.34 \tag{20.e}$$

$$G_8 = -4.57 \times 10^6 \qquad \beta > 5.34 \tag{20.f}$$

The value of β used to define G_7 and G_8 is lagged in time.

The final model with pressure gradient modifications, called MMLPG, was developed using the equilibrium turbulent flows of Bradshaw and is defined by equations (13) through (20). The resulting velocity-defect profiles for all three pressure gradient flows are shown in figure 15 and exhibit good agreement with the experimental data, with the exception of the strong pressure gradient case. The calculations were performed on a CRAY Y-MP computer and the computational times are given in table 2. The strong pressure gradient case took considerably longer to reach convergence because the code had difficulties resolving oscillations induced at the upstream boundary, which used a fixed velocity profile for the inflow boundary condition.

Averaging for Multiple Boundaries

If both walls in a given coordinate direction are solid surfaces, the turbulent mixing lengths are computed separately at each surface and then averaged. The Sajben diffuser, which is described in the next section, has solid walls at the upper and lower vertical boundaries, and is a typical example of a geometry which would require averaging of the mixing length. The averaging formula of Appendix A, equation (A.10), which was used to average the F_{wake} function in the Baldwin-Lomax model, is also used here to average the mixing length:

$$l = \frac{l_1 f_1 + l_2 f_2}{f_1 + f_2} \qquad (21)$$

If the lower and upper boundaries in the vertical direction, are solid surfaces, as in the Sajben diffuser, then l_1 and l_2 are the mixing lengths at the lower and upper boundaries, respectively. The functions f_1 and f_2 are defined in equation (A.11) of Appendix A.

Adverse Pressure Gradient Test Cases

To evaluate MMLPG for some typical propulsion flows, a converging-diverging duct, referred to as the Sajben diffuser, was used. This duct was designed to be representative of the diffuser portion of the inlet for a rocket/ramjet propulsion system. Detailed experimental and computational data are available for flows with and without external excitations.[22-27] This study, however, dealt only with the unexcited flows. The geometry of the diffuser is given in figure 16: the throat height, H, is 44 mm; the entrance-to-throat height ratio is 1.4, and the exit-to-throat height ratio is 1.5. The grid, shown in figure 17, is the same as that used by references 1 and 26, and has 81 streamwise points and 51 vertical points. It was packed in the vertical direction near the walls in order to resolve the turbulent boundary layers and in the streamwise direction near the throat to resolve the strong gradients. The reliability of this grid is discussed in Appendix B. Three transonic flow cases were run. The flowfields were determined by setting R, the ratio of the exit static pressure to the inlet total pressure. The first case had a weak normal shock with R=0.82; the second case had subsonic flow throughout (no shock) with R=0.862, and the third case had a strong normal shock with R=0.72. The reference velocity, temperature, pressure and length used in Proteus were 4.72 m/s, 292 K, 135 kPa, and .044 m respectively. These values match the values used in other numerical simulations of this flow.[1, 24, 26] The initial conditions were zero velocity and constant temperature and pressure everywhere in the flow field. Both cases were run using MMLPG and the Baldwin-Lomax model.

Weak Shock Case

The weak shock case was used as an example case in the Proteus User's Manual,[1] and therefore was run first in order to gain familiarity with running this type of flow. It was computed as described in reference 1: First the exit pressure was gradually reduced to R = 0.1338 to establish supersonic flow throughout the diffuser; then it was gradually raised to R = 0.82, the desired ratio to establish the weak normal shock, and iterated until the solution was no longer changing appreciably with time. A plot of the static pressure on the top wall at two locations, one upstream and one downstream of the normal shock, as the solution progresses is shown in figure 18. This indicates that pressure reaches a steady state level, which, for practical engineering purposes, can be considered a converged solution. A closer examination of the results indicates that the solution oscillates slightly about a mean steady level. This may be caused by inherent unsteadiness in the flow; Salmon et al.[22] mention that very low-amplitude, self-sustaining oscillations were observed experimentally. It is more likely, however, that the oscillations present in this calculation are numerical in nature, which is common for flows with shock waves. The oscillations originating at the shock may not be damped out by the artificial viscosity and therefore tend to migrate upstream. The artificial viscosity used in Proteus to calculate this flow was second- and fourth-order explicit, both using the nonlinear coefficient model of Jameson et al.;[28] the respective smoothing coefficients are κ_2 and κ_4, as given in Appendix B. For the entire calculation, κ_2 was set to 0.1; κ_4 was set to .005 for the first 6000 iterations, while the exit pressure was changing, and decreased to .0004 for the remaining 3000 iterations, which were at a constant exit pressure. More details about the effects of the artificial viscosity on this solution are provided in Appendix B.

The static pressure distribution on the top and bottom walls is given in figure 19. The shock location on the upper wall and the shock Mach number at the edge of the upper wall boundary layer are given in table 3. Both MMLPG and BLM accurately predict the pressure distribution on the wall and the location of the shock. Each case was run for 9000 iterations and calculations made using MMLPG and BLM required 3.44×10^{-5} sec/iteration/grid point and 3.36×10^{-5} sec/iteration/grid point respectively on the CRAY Y-MP computer.

No Shock Case

The second diffuser test case did not have a normal shock wave. To compute this case, the exit pressure was gradually lowered to R=0.862 then iterated until the solution stopped changing. A steady state solution was reached with subsonic flow throughout the entire diffuser. The Proteus default artificial viscosity, which uses the constant coefficient model of Steger[29] with both fourth-order explicit and second-order implicit artificial viscosity, was used; the smoothing coefficients, $\varepsilon_E^{(4)}$ and ε_I (defined in Appendix B), had values of 1.0 and 2.0, respectively.

The static pressure distribution on the top and bottom walls is shown in figure 20 and indicates that MMLPG is clearly better than BLM at predicting the pressure distribution, though it still predicts a larger pressure drop than that indicated by the experimental data. The MMLPG results are similar to the calculations of Hsieh et al[25] who attributed the lower throat pressure to the fact that the experiment was highly sensitive to small perturbations in exit pressure. The maximum Mach numbers in the diffuser are given in table 4. Although no experimental data is available to compare these values, the MMLPG results are in best agreement with the calculations of Georgiadis[27] who used the PARC Navier-Stokes code[30] for the same geometry. Of the three diffuser test cases, this flow is most similar to the benchmark cases used to derive MMLPG, although its pressure gradients are stronger, and indicates that MMLPG is capable of computing the flows for which it was designed. Each case was run for 9000 iterations and calculations using MMLPG and BLM required 3.45×10^{-5} sec/iteration/grid point and 3.36×10^{-5} sec/iteration/grid point, respectively, on the CRAY Y-MP computer.

Strong Shock Case

The final diffuser flow computed was the case with a strong normal shock positioned in the throat. This case was run in a manner similar to the weak shock case: First the exit pressure was gradually lowered to R=0.1338 to achieve supersonic flow throughout the diffuser; then it was gradually raised to R=0.72 to establish the strong normal shock in the throat region, and iterated there until the solution stopped changing appreciably with time. Proteus was run in both steady and unsteady modes to try to simulate the experimentally observed self-excited oscillations of 217 Hz.[22] Unsteady mode in Proteus is achieved by calculating a global time step whereas steady mode uses a local time step to speed up the computation. Neither calculation simulated the experimentally observed oscillatory behavior, but instead produced very small numerical oscillations in the flow properties. (The artificial viscosity used for the strong shock calculations was the same as that used for the weak shock calculation.) Figure 21 shows the static pressure on the top wall at the experimental shock location and illustrates the behavior of these small oscillations; the calculation shown was run in unsteady mode with MMLPG.

The static pressure on the top and bottom walls are presented in figure 22 and the shock location and Mach number at the edge of the top wall boundary layer are given in table 5. Both MMLPG and BLM predicted the shock location too far downstream. The experiment predicted a region of separation on the top wall just downstream of the shock with the flow reattaching at x/H=6.0. MMLPG predicted a very small region of separation on the top wall which reattached at x/H=3.6. BLM predicted very small regions of separation on both the top and bottom walls which reattached at x/H=3.8 and x/H=6.2. The separated behavior is illustrated in figure 23, which gives the velocity profiles at four locations downstream of the shock. These peculiar results can be attributed to the fact that both MMLPG and BLM compute very high values of μ_t due to the large increase in vorticity downstream of the shock. The poor performance of both models for this case can also be attributed to the fact that all of the models are equilibrium turbulence being used to calculate a flow which is clearly nonequilibrium. The inadequate performance of MMLPG for the strong shock case is also explained by the derivation of the model, which is based on experimental data for beta values between 0 and 5, while this flow encountered β values as high as 12,000. Each case was run for 10,000 iterations and the steady calculations using MMLPG and BLM required 3.54×10^{-5} sec/iteration/grid point and 3.82×10^{-5} sec/iteration/grid point, respectively, on the CRAY Y-MP computer.

Summary and Conclusions

In the current work, the range of applicability of the MML algebraic turbulence model was extended to calculate more general boundary layer flows with zero and adverse pressure gradients. To accomplish this objective, MML was first modified to predict the appropriate boundary layer growth with increasing Re_x by incorporating a relationship for the mixing length as a function of the local skin friction coefficient. Using the experimental data of Bradshaw for zero, mild and strong adverse pressure gradient flows, modifications were also added to account for adverse pressure gradient effects. The resulting generalized model, called MMLPG, accurately predicted zero and adverse pressure gradient flows over a plate and exhibited better agreement with experimental data than the Baldwin-Lomax model.

To more thoroughly evaluate MMLPG for other adverse pressure gradient flows, this model was also used to calculate three transonic diffuser flow test cases: flow with a weak shock, flow with no shock, and flow with a strong shock. For the weak-shock case, MMLPG and BLM did equally well in predicting the shock Mach number and location, and also in predicting the static pressure distribution on the top and bottom diffuser walls. For the no shock case, MMLPG was significantly better than the Baldwin-Lomax model at predicting the static pressures on the walls and at predicting the

maximum Mach number in the duct. Both models inadequately predicted the strong shock flow, over-predicting the shock Mach number and location and under predicting the size of the separation on the top wall. In addition, BLM predicted a small separation on the bottom wall, although no separation was observed there experimentally. This strong shock flow over-stepped the bounds of the assumptions made in the development of both of these equilibrium turbulence models.

Overall, the flat plate and transonic diffuser results indicate that MMLPG is capable of accurately predicting turbulent flows with and without adverse pressure gradients. Future work should include continued validation of the model for these types of flows as well as continued development of the model to better account for stronger adverse pressure gradient flows both with and without separation.

References

1. Towne, C. E., Schwab, J. R. and Bui, T. T., "Proteus Two-Dimensional Navier-Stokes Computer Code, Version 2.0, Vols. 1-3," NASA TM 106336, 106337, 106339, October 1993.

2. Briley, W. R., McDonald, H., "Solution of the Multidimensional Compressible Navier-Stokes Equations by a Generalized Implicit Method," *Journal of Computational Physics*, Vol. 24, 1977, pp. 373-397.

3. Beam, R. M. and Warming, R. F., "An Implicit Factored Scheme for the Compressible Navier-Stokes Equations," *AIAA Journal*, Vol. 16, No. 4, April 1978, pp. 393-402.

4. Baldwin, B. and Lomax, H., "Thin Layer Approximation and Algebraic Model for Separated Turbulent Flows," AIAA Paper 78-257, January 1978.

5. Chien, K. Y., "Prediction of Channel and Boundary-Layer Flows with a Low-Reynolds-Number Turbulence Model," *AIAA Journal*, Vol. 20, No. 1, January 1982, pp. 33-38.

6. Potapczuk, M. G., "Navier-Stokes Analysis of Airfoils with Leading Edge Ice Accretions," Ph.D. Dissertation, University of Akron, May 1989.

7. Yu, N. J., Allmaras, S. R., and Moschetti, K. G., "Navier-Stokes Calculations for Attached and Separated Flows Using Different Turbulence Models," AIAA Paper 91-1791, June 1991.

8. Visbal, M. and Knight, D., "The Baldwin-Lomax Turbulence Model for Two-Dimensional Shock-Wave/Boundary-Layer Interactions," *AIAA Journal*, Vol. 22, No. 7, July 1984, pp. 921-928.

9. Kirtley, K. R., "A Coupled, Parabolic-Marching Method for the Prediction of Three-Dimensional Viscous Incompressible Turbomachinery Flows," Ph. D. Thesis, Pennsylvania State University, December, 1987.

10. Degani, D. and Schiff, L. B., "Computation of Turbulent Supersonic Flows around Pointed Bodies Having Crossflow Separation," *Journal of Computational Physics*, Vol. 66, 1986, pp. 173-196.

11. Menter, F. R., "Performance of Popular Turbulence Models for Attached and Separated Adverse Pressure Gradient Flows," *AIAA Journal*, Vol. 30, No. 8, August 1992, pp. 2066-2072.

12. Stock, H. W. and Haase, W., "The Determination of Turbulent Length Scales in Algebraic Turbulence Models for Attached and Slightly Separated Flows Using Navier-Stokes Methods," AIAA Paper 87-1302, June 1987.

13. Sakowski, B., Darling, D., Roach, R. L. and van de Wall, A., "Evaluation and Application of the Baldwin-Lomax Turbulence Model in Two-Dimensional, Unsteady, Compressible Boundary Layers with and without Separation in Engine Inlets," AIAA Paper 92-3676, July 1992.

14. Chima, R. V., Giel, P. W. and Boyle, R. J., "An Algebraic Turbulence Model for Three-Dimensional Viscous Flows," NASA TM 105931, January 1993.

15. Bradshaw, P., "The Turbulence Structure of Equilibrium Boundary Layers," NPL Aero Report 1184, January, 1966.

16. Cebeci, T. and Smith, A. M. O., *Analysis of Turbulent Boundary Layers*, Academic Press, New York, 1974.

17. Launder, B. E. and Priddin, C. H., "A Comparison of Some Proposals for the Mixing Length Near a Wall," *International Journal of Heat and Mass Transfer*, Vol. 16, 1973, pp. 700-702.

18. Musker, A. J., "Explicit Expression for the Smooth Wall Velocity Distribution in a Turbulent Boundary

Layer," *AIAA Journal*, Vol. 17, No. 6, June 1979, pp. 655-657.

19. Clauser, F. H., "Turbulent Boundary Layers in Adverse Pressure Gradients," *Journal of Aeronautical Sciences*, February 1954, pp. 91-108.

20. Weighardt, K., "Flat Plate Flow. u_∞=33 m/sec," Proceedings, AFOSR-IFP-Stanford Conference on Computation of Turbulent Boundary Layers-1968, Vol. II, Ed. by Coles, D.E. and Hirst, E. A., 1968, pp. 98-123.

21. White, F. M., *Viscous Fluid Flow*, McGraw-Hill, Inc., New York, 1991.

22. Salmon, J. T., Bogar, T. J. and Sajben, M., "Laser Doppler Velocimeter Measurements in Unsteady, Separated, Transonic Diffuser Flows," *AIAA Journal*, Vol. 21, No. 12, 1983, pp. 1690-1697.

23. Bogar, T. J., Sajben, M. and Kroutil, J. C., "Characteristic Frequencies of Transonic Diffuser Flow Oscillations," *AIAA Journal*, Vol. 21, No. 9, 1983, pp. 1232-1240.

24. Hsieh, T., Bogar, T. J. and Coakley, T. J., "Numerical Simulation and Comparison with Experiment for Self-Excited Oscillations in a Diffuser Flow," *AIAA Journal*, Vol. 25, No. 7, 1987, pp. 936-943.

25. Hsieh, T., Wardlaw, A. B. Jr., Collins, P. and Coakley, T., "Numerical Investigation of Unsteady Inlet Flowfields," *AIAA Journal*, Vol. 25, No. 1, January 1987, pp. 75-81.

26. Bui, T. T., "Implementation/Validation of a Low Reynolds Number Two-Equation Turbulence Model in the Proteus Navier-Stokes Code — Two-Dimensional/Axisymmetric," NASA TM 105619, April 1992.

27. Georgiadis, N. J., "An Evaluation of Turbulence Models for Propulsion Flows," Master's Thesis, University of Akron, May 1993.

28. Jameson, A., Schmidt, W. and Turkel, E., "Numerical Solutions of the Euler Equations by Finite Volume Methods Using Runge-Kutta Time-Stepping Schemes," AIAA Paper 81-1259, June 1981.

29. Steger, J. L., "Implicit Finite-Difference Simulation of Flow about Arbitrary Two-Dimensional Geometries," *AIAA Journal*, Vol. 16, No. 7, July 1978, pp. 679-686.

30. Cooper, G. K. and Sirbaugh, J. R., "PARC Code: Theory and Usage," Arnold Engineering Development Center Report AEDC-TR-89-15, December 1989.

31. Pulliam, T. H., "Artificial Dissipation Models for the Euler Equations," *AIAA Journal*, Vol. 24, No. 12, December 1986, pp. 1931-1940.

Appendices

Appendix A: The Baldwin-Lomax Turbulence Model

A generalized version of the Baldwin-Lomax algebraic turbulence model[4] is available in Proteus.[1] The turbulent shear and normal stresses and the turbulent heat flux are modeled using the Boussinesq approach, where the effective viscosity is defined as $\mu_{eff} = \mu + \mu_t$, the second coefficient of viscosity is defined as $\lambda_{eff} = \lambda + \lambda_t$, and the effective thermal conductivity coefficient is defined as $k_{eff} = k + k_t$.

For wall bounded flows, the Baldwin-Lomax model is a two-layer model:

$$\mu_t = \begin{cases} (\mu_t)_{inner}, & y \le y_{crossover} \\ (\mu_t)_{outer}, & y > y_{crossover} \end{cases} \qquad (A.1)$$

where $y_{crossover}$ is smallest value of y at which the inner and outer region values of μ_t are equal. For free turbulent flows, $\mu_t = (\mu_t)_{outer}$.

1. Inner Region

The inner region turbulent viscosity is computed from

$$(\mu_t)_{inner} = \rho l^2 |\omega| \qquad (A.2)$$

where l is the mixing length given by

$$l = \kappa y \left(1 - e^{-\frac{y^+}{A^+}} \right) \qquad (A.3)$$

The quantity $|\omega|$ is the magnitude of the total vorticity, defined for two-dimensional planar flow as

$$|\omega| = \left|\frac{\partial v}{\partial x} - \frac{\partial u}{\partial y}\right| \tag{A.4}$$

2. Outer Region

In the outer region, the turbulent viscosity is given by

$$(\mu_t)_{outer} = KC_{cp}\rho F_{Kleb} F_{wake} \tag{A.5}$$

where K is the Clauser constant, taken as 0.0168 and C_{cp} is a constant taken as 1.6. The quantity F_{wake} is computed from

$$F_{wake} = \begin{cases} y_{max} F_{max} & \text{for wall bounded flows} \\ C_{wk} V_{diff}^2 \dfrac{y_{max}}{F_{max}} & \text{for free turbulent flows} \end{cases} \tag{A.6}$$

where the constant C_{wk} is 0.25 and

$$V_{diff} = |\vec{V}|_{max} - |\vec{V}|_{min} \tag{A.7}$$

where $\vec{V}$ is the total velocity vector. The quantity F_{max} is the maximum value of

$$F(y) = \begin{cases} y|\omega| \left(1 - e^{-\frac{y^+}{A^+}}\right) & \text{for wall bounded flows} \\ y|\omega| & \text{for free turbulent flows} \end{cases} \tag{A.8}$$

and y_{max} is the value of y corresponding to F_{max}. F_{Kleb} is the Klebanoff intermittency factor which accounts for the experimentally observed phenomenon that as the free stream is approached, the fraction of time the flow is turbulent decreases. It is given by

$$F_{Kleb} = \left[1 - 5.5\left(\frac{C_{Kleb} y}{y_{max}}\right)^6\right]^{-1} \tag{A.9}$$

where C_{Kleb} is a constant taken as 0.3.

3. Multiple Boundaries

If both walls in a given coordinate direction are solid surfaces, the turbulence model equations are applied separately at each surface and then averaged. The two outer regions overlap, and it assumed that the two inner regions do not overlap. The averaging procedure deals with the F_{wake} function. For example, in the vertical direction, if the upper and lower boundaries are both solid surfaces, the two values of F_{wake} at a particular streamwise station are combined using the following averaging formula:

$$F_{wake} = \frac{(F_{wake})_1 f_1 + (F_{wake})_2 f_2}{f_1 + f_2} \tag{A.10}$$

The quantities $(F_{wake})_1$ and $(F_{wake})_2$ are the separate values computed at the lower and upper boundaries using equation (A.6). The functions f_1 and f_2 are defined by

$$f_1 = \left(\frac{2D_1}{y_1}\right)^n \qquad f_2 = \left(\frac{2D_2}{y_2}\right)^n \tag{A.11}$$

The constant n is set equal to 2.0, y_1 and y_2 are the normal distances to the bottom and top surfaces, respectively, and D_1 and D_2 are the normal distances from the two surfaces to the location of $|\vec{V}|_{max}$. In addition, the y/y_{max} value used in equation (A.9) for F_{Kleb} is computed for both surfaces and the minimum value is used. These values of F_{Kleb} and F_{wake} are then used in equation (A.5) to compute $(\mu_t)_{outer}$.

Appendix B: Artificial Viscosity and Grid Convergence

High frequency nonlinear instabilities can appear as the Proteus solution develops. For example, physical phenomena, such as shock waves, can cause instabilities when they are captured by the finite difference algorithm. In addition, high Reynolds number flows may have oscillations resulting from the odd-even decoupling inherent in the use of central spatial differencing of the convective terms. Artificial viscosity may be used to suppress these oscillations. The two artificial viscosity models in Proteus are the constant coefficient model of Steger[29] and the nonlinear coefficient model of Jameson et al.[28] The implementation of these models in generalized nonorthogonal coordinates was taken from Pulliam.[31]

1. Constant Coefficient Model

The constant coefficient model uses a combination of explicit and implicit smoothing. The standard explicit artificial viscosity uses fourth-order differences. Second-order explicit artificial viscosity, which provides more smoothing, is also available in Proteus, however it is rarely used because it introduces a large

error. The implicit smoothing is second order and is used to extend the linear stability bound of the fourth-order explicit smoothing.

The explicit artificial viscosity is implemented in the Proteus alternating direction implicit (ADI) algorithm[2] by adding the following terms to the right-hand side source term for the first ADI sweep. (The governing equations of Proteus are given in detail in reference 1.)

$$\frac{\varepsilon_E^{(2)}\Delta t}{J}(\nabla_\xi\Delta_\xi Q+\nabla_\eta\Delta_\eta Q)-\frac{\varepsilon_E^{(4)}\Delta t}{J}[(\nabla_\xi\Delta_\xi)^2Q+(\nabla_\eta\Delta_\eta)^2Q] \tag{B.1}$$

where $\varepsilon_E^{(2)}$ and $\varepsilon_E^{(4)}$ are the second- and fourth-order explicit artificial viscosity coefficients, ξ and η are the computational coordinate directions, Q is the vector of dependent variables and J is the Jacobian of the coordinate transformation. The symbols ∇ and Δ are the standard backward and forward first difference operators.

The implicit artificial viscosity is implemented by adding the following terms to the left-hand side of the governing equation.

$$-\frac{\varepsilon_I\Delta t}{J}\left[\nabla_\xi\Delta_\xi(J\Delta\hat{Q}^*)\right] \tag{B.2a}$$

$$-\frac{\varepsilon_I\Delta t}{J}\left[\nabla_\eta\Delta_\eta(J\Delta\hat{Q}^n)\right] \tag{B.2b}$$

Equation (B.2a) is added for the first ADI sweep and equation (B.2b) is added for the second ADI sweep. The constant ε_I is the implicit artificial viscosity coefficient.

The optimum values of the coefficients $\varepsilon_E^{(2)}$, $\varepsilon_E^{(4)}$ and ε_I vary from problem to problem. They should be small so as not to corrupt the physical solution, yet large enough to damp any instabilities. The Proteus User's Guide[1] recommends starting values of $\varepsilon_E^{(4)}=1.0$, $\varepsilon_E^{(2)}=1.0$ and $\varepsilon_I=2.0$.

2. Nonlinear Coefficient Model

The nonlinear coefficient artificial viscosity is explicit and contains second and fourth-order differences. The following terms are added to the right-hand side of the governing equations.

$$\nabla_\xi\{\left[\left(\frac{\psi}{J}\right)_{i+1}+\left(\frac{\psi}{J}\right)_i\right](\varepsilon_\xi^{(2)}\Delta_\xi Q-\varepsilon_\xi^{(4)}\Delta_\xi\nabla_\xi\Delta_\xi Q)_i\}+\nabla_\eta\{\left[\frac{\psi}{J_{j+1}}+\frac{\psi}{J_j}\right](\varepsilon_\eta^{(2)}\Delta_\eta Q-\varepsilon_\eta^{(4)}\Delta_\eta\nabla_\eta\Delta_\eta Q)_j\} \tag{B.3}$$

The expression ψ is given by

$$\psi=\psi_x+\psi_y \tag{B.4}$$

where ψ_x and ψ_y are spectral radii defined by

$$\psi_x=\frac{|U|+a\sqrt{\xi_x^2+\xi_y^2}}{\Delta\xi}$$
$$\psi_y=\frac{|V|+a\sqrt{\eta_x^2+\eta_y^2}}{\Delta\eta} \tag{B.5}$$

The second- and fourth- order nonlinear artificial viscosity coefficients are a function of the pressure field. In the ξ direction, they are given by

$$(\varepsilon_\xi^{(2)})_i=\kappa_2\Delta t\ \max(\sigma_{i+1},\sigma_i,\sigma_{i-1}) \tag{B.6a}$$

$$(\varepsilon_\xi^{(4)})_i=\max\left[0,\kappa_4\Delta t-(\varepsilon_\xi^{(2)})_i\right] \tag{B.6b}$$

where

$$\sigma_i=\left|\frac{p_{i+1}-2p_i+p_{i-1}}{p_{i+1}+2p_i+p_{i-1}}\right| \tag{B.7}$$

Similar formulas are used in the η direction.

The parameter σ is a pressure gradient scaling parameter which increases the amount of second-order smoothing relative to fourth-order near shock waves. The parameters κ_2 and κ_4 are user-specified constants. As with the constant coefficient model, the optimum values of κ_2 and κ_4 are problem dependent. Typical values range from $\kappa_4=0.005$ and $\kappa_2=0.01$ for flows with no shocks, to $\kappa_4=0.0004$ and $\kappa_2=0.1$ for flows with shocks.[1] Pulliam gives $\kappa_2=0.25$ and $\kappa_4=0.01$ as typical values for an Euler analysis.[1, 31]

3. Comments on Artificial Viscosity

As previously mentioned, artificial viscosity is generally used to minimize oscillations which occur when computing high Reynolds number flows and flows with shock waves. The artificial viscosity coefficients should be as small as possible so as not to corrupt the solution, yet large enough to damp the nonphysical instabilities. Optimum values of the artificial viscosity

coefficients vary from problem to problem; the coefficients used to calculate the flows presented herein were selected based on values used for similar cases, as given in the Proteus User's Manual.[1] Some representative test cases were evaluated to insure that the chosen artificial viscosity did not corrupt the physical characteristics of the flow.

The flat plate flows were run using the constant coefficient model with $\varepsilon_E^{(4)}=1.0$, $\varepsilon_E^{(2)}=0.0$ and $\varepsilon_I=2.0$. For these flows, it was possible to run Proteus with zero artificial viscosity, however the solutions took two to four times longer to converge. Upon close examination, these solutions did not agree as closely with experimental data as the solutions computed using artificial viscosity.

For the diffuser flows, the artificial viscosity effects were examined for the weak shock case. As mentioned earlier, the nonlinear coefficient model was used. A value of $\kappa_2=0.1$ was used for the entire calculation, with $\kappa_4=0.005$ while the exit pressure was changing (i.e, for the first 6000 iterations), and $\kappa_4=0.0004$ for the remaining 3000 iterations, which were at a constant exit pressure. It was not possible to compute this flow without artificial viscosity, so the effect of doubling and halving the smoothing coefficients was examined. The static pressure distribution on the top and bottom walls for this comparison (computed using MMLPG) is given in figure 24. The solution computed using half of the original artificial viscosity was nearly identical to the original solution, indicating that the originally chosen artificial viscosity is reasonable for this flow. Doubling the artificial viscosity gave a less desirable result in that the normal shock was smeared over a greater number of grid points.

4. Grid Convergence

Grid convergence is an important factor in the accuracy of a CFD calculation. The grids used to make the flat plate and transonic diffuser calculations were assessed to insure their grid independence. For the zero pressure gradient flat plate calculations, a 101x101 grid was initially chosen. The size of this grid was systematically reduced in each direction in order to find the coarsest grid that would give a solution which would not change if additional grid points were added. The 51x51 grid shown in figure 5 was chosen based on this procedure.

The grid used to make the transonic diffuser calculations had been used previously by others,[1, 26] so it is probable that this grid gives a reliable solution. As an added check, the number of grid points in each direction was doubled, and the resulting 162x101 grid was used to compute the no shock flow using MMLPG. A comparison of these results with the results obtained using the 81x51 grid of figure 17 is given in figure 25 and indicates that the 81x51 grid is reliable.

Table 1. Parameters used in pressure gradient modifications.

Pressure Gradient Strength	β	G_3	G_5	G_6
zero	0	1.00	23,300	-7.75×10^{6}
mild	1	1.25	30,100	-1.16×10^{7}
strong	5	1.53	33,800	-2.09×10^{7}

Table 2. Computational times for flat plate flows.

(a) Zero Pressure Gradient

Model	Iterations	sec./iter./grid point
BLM	2000	2.02×10^{-5}
MMLPG	2000	2.00×10^{-5}

(b) Mild Pressure Gradient

Model	Iterations	sec./iter./grid point
BLM	3000	2.14×10^{-5}
MMLPG	3000	2.17×10^{-5}

(c) Strong Pressure Gradient

Model	Iterations	sec./iter./grid point
BLM	18,000	2.14×10^{-5}
MMLPG	10,000	1.96×10^{-5}

Table 3. Shock location and Mach number, weak shock case.

Turbulence Model	Shock Mach Number	Shock Location (x/H)
MMLPG	1.233	1.57
BLM	1.228	1.49
Experiment[22]	1.235	1.41

Table 4. Maximum Mach number, no shock case

Turbulence Model	Maximum Mach Number
MMLPG	0.881
BLM	0.976

Table 5. Shock location and Mach number, strong shock case.

Turbulence Model	Shock Mach Number	Shock Location (x/H)
MMLPG	1.626	3.13
BLM	1.665	2.90
Experiment[22]	1.353	1.98

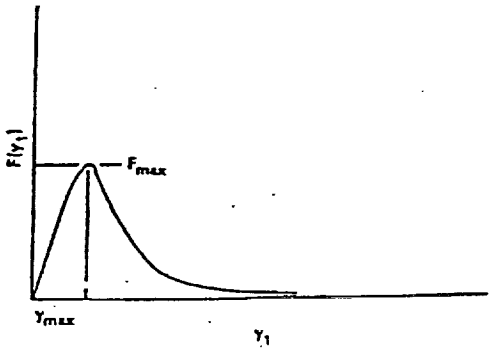

(a) Attached flow

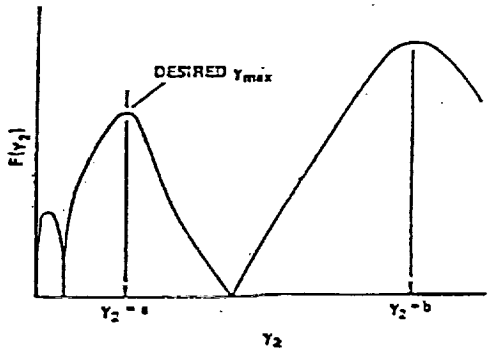

(b) Separated flow

Figure 1. Baldwin-Lomax F(y) profiles.

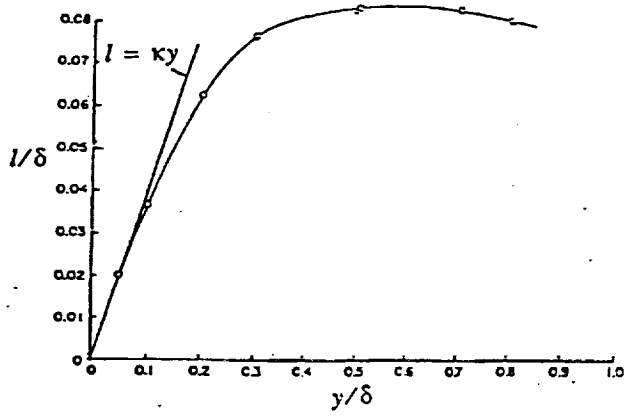

Figure 2. Dimensionless mixing length distribution across a turbulent boundary layer.[16]

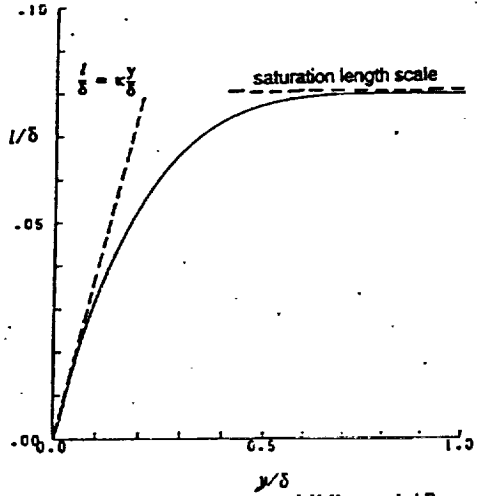

Figure 3. Mixing length profile for MML model.[6]

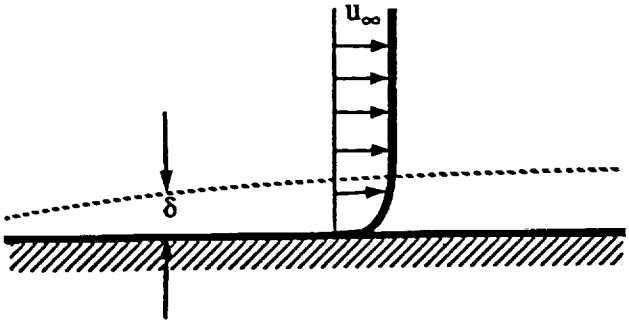

Figure 4. Illustration of flow over a flat plate.

Figure 5. Computational grid for zero pressure gradient flat plate case

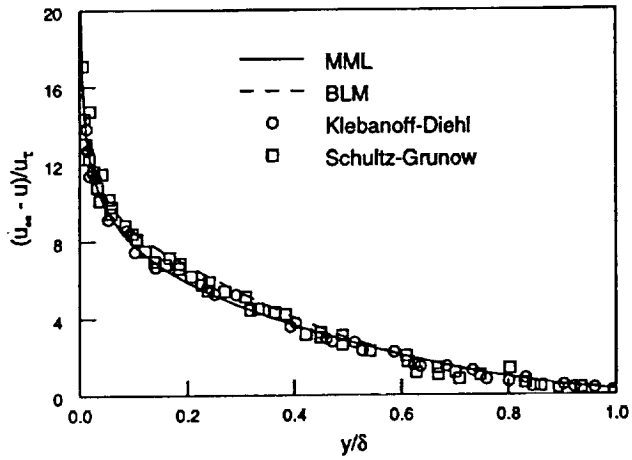

Figure 6. Velocity-defect profiles for zero pressure gradient flow, Re_x=7x10^6.

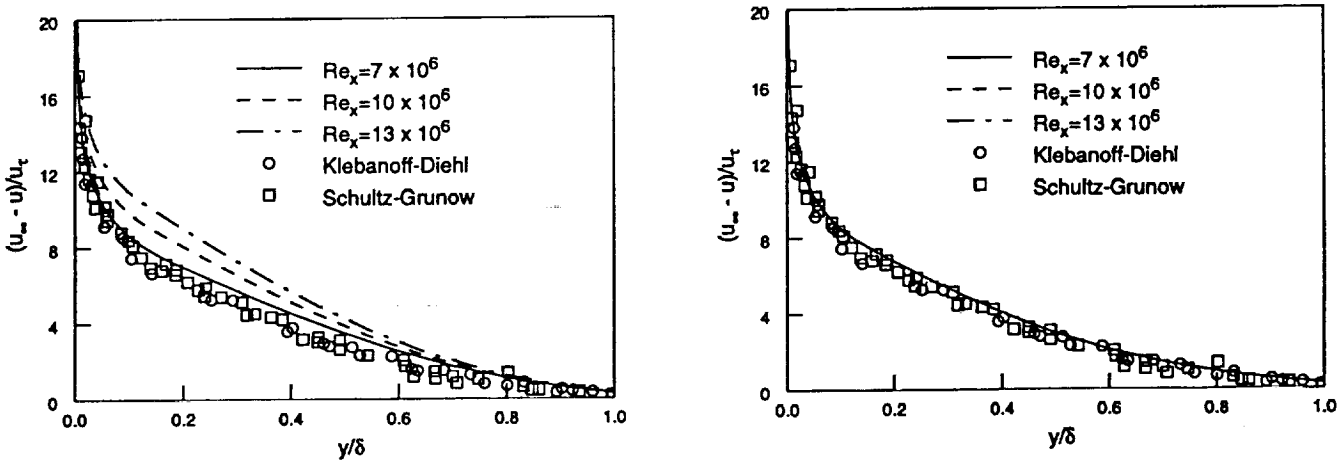

(a) MML (b) BLM

Figure 7. Velocity-defect profiles for zero pressure flow at three Reynolds numbers.

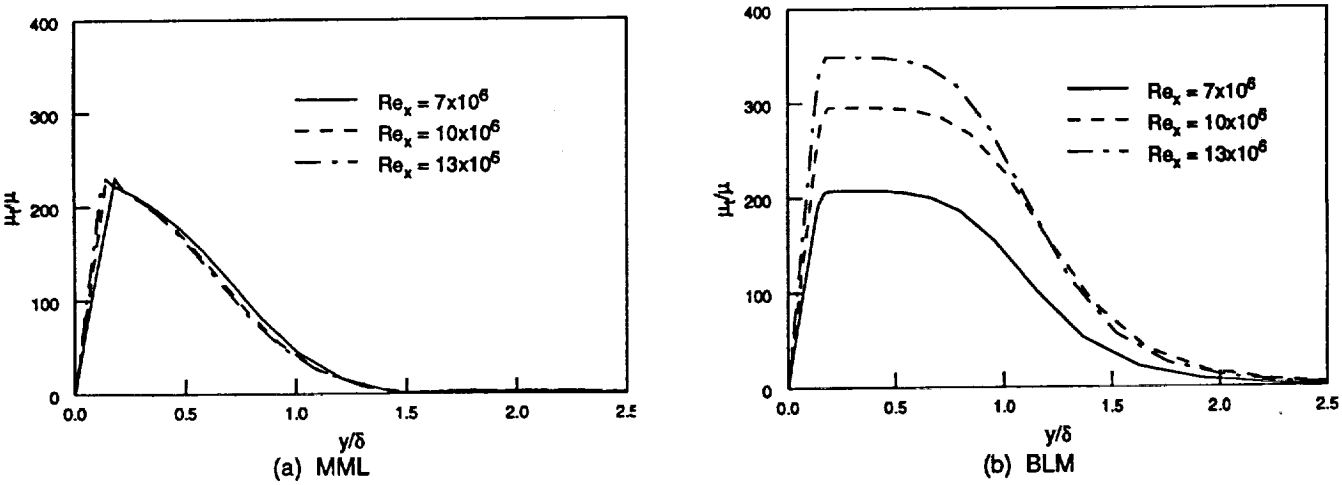

(a) MML (b) BLM

Figure 8. Turbulent viscosity for zero pressure gradient flat plate flow at three Reynolds numbers.

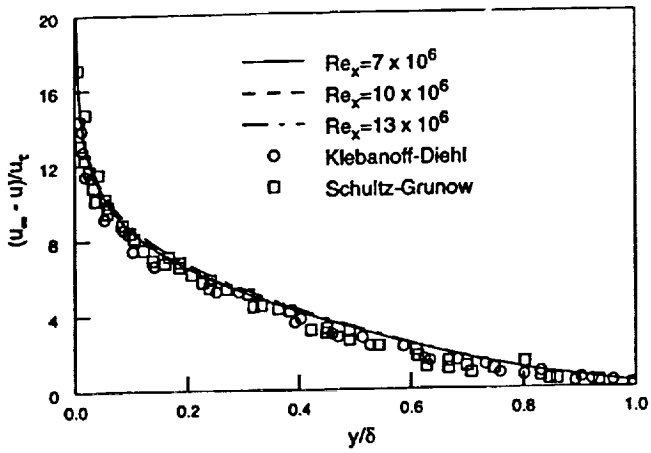

Figure 9. Velocity-defect profiles for zero pressure gradient flow; MML of equations (9) and (11).

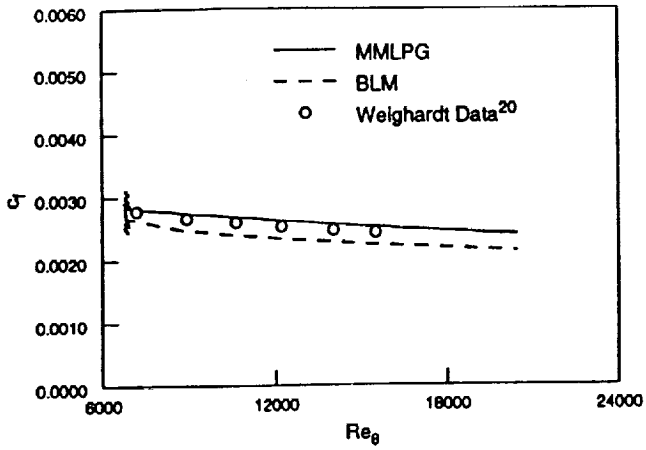

Figure 10. Local skin friction coefficient for zero pressure gradient flow: MML of equations (9) and (11).

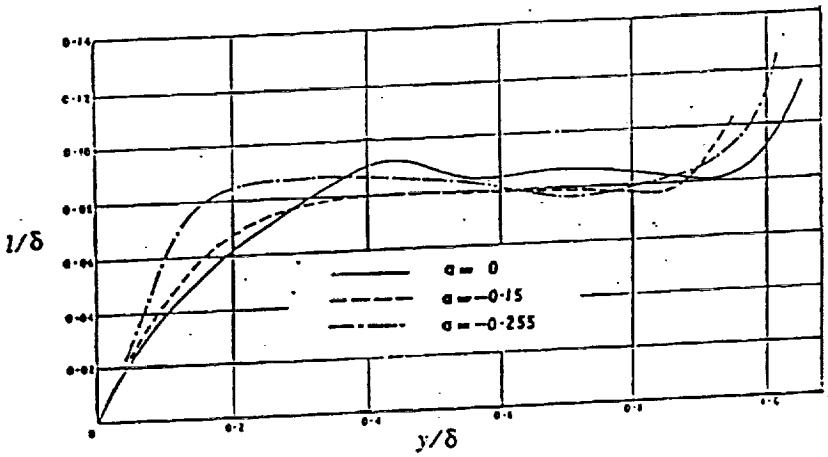

Figure 11. Mixing length profiles at three pressure gradients.[15]

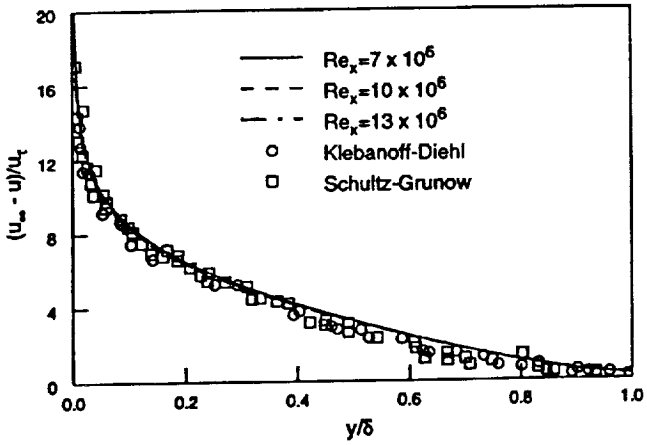

Figure 12. Velocity-defect for zero pressure gradient flow; MML of equations (13) through (17).

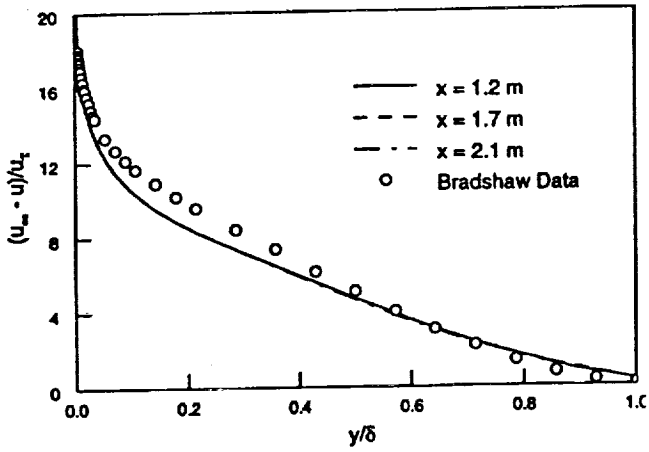

(a) MML of equations (13) through (17)

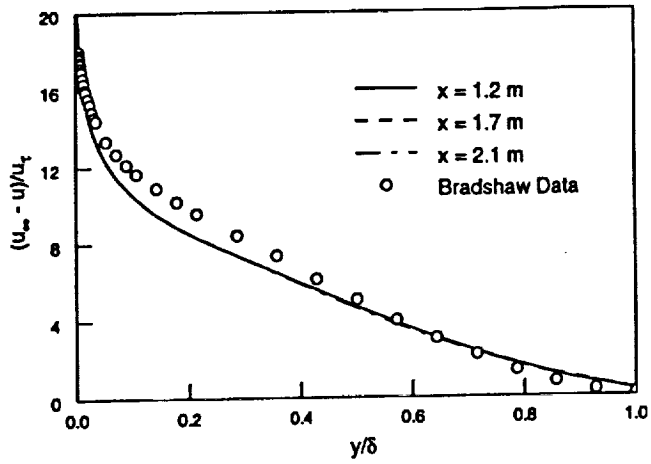

(b) BLM

Figure 13. Velocity-defect for mild pressure gradient flow.

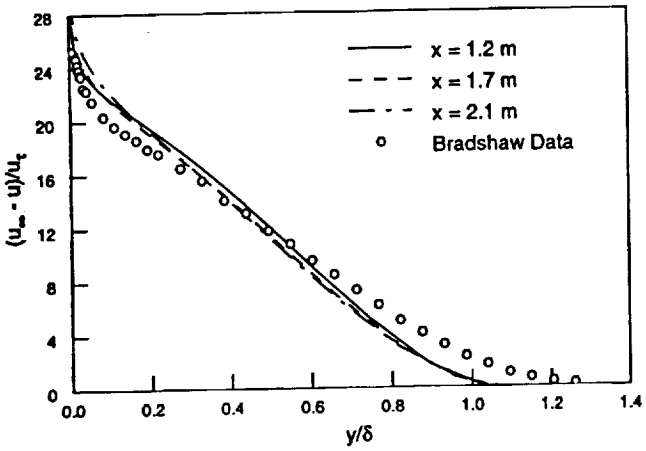

(a) MML of equations (13) through (17)

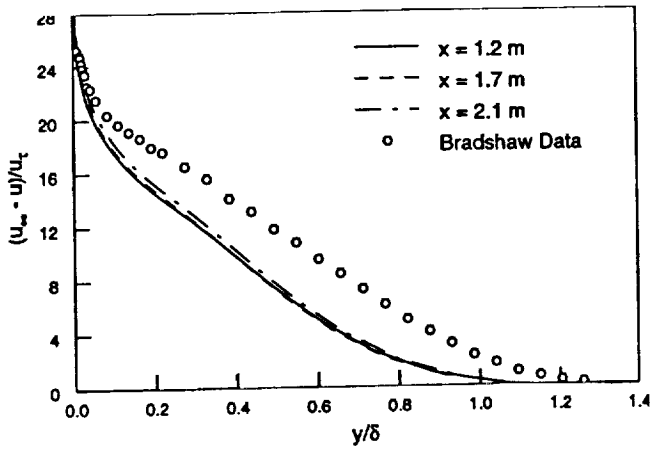

(b) BLM

Figure 14. Velocity-defect for strong pressure gradient flow.

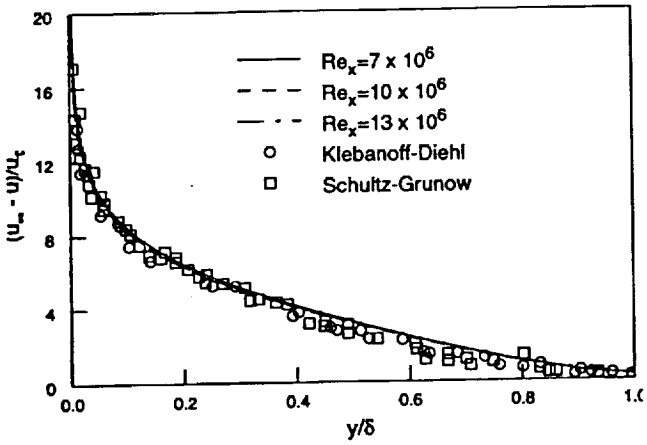

(a) Zero pressure gradient

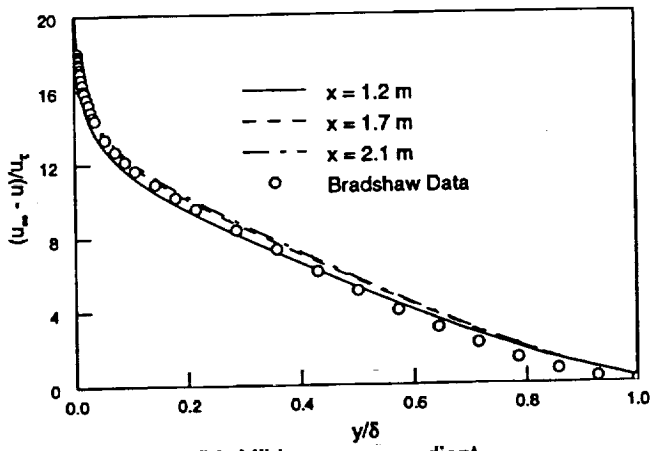

(b) Mild pressure gradient

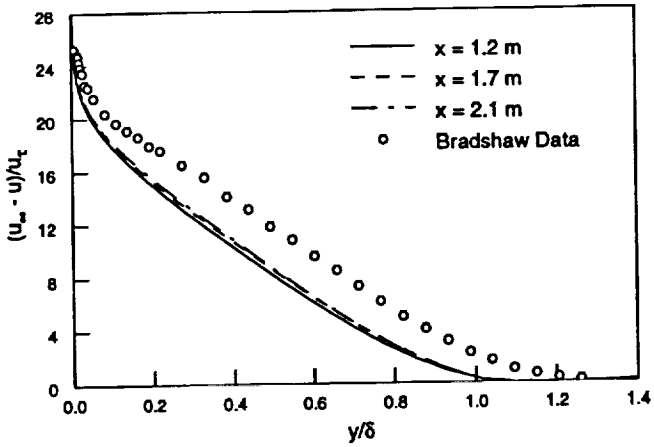

(c) Strong pressure gradient

Figure 15. Velocity-defect profiles computed using MMLPG.

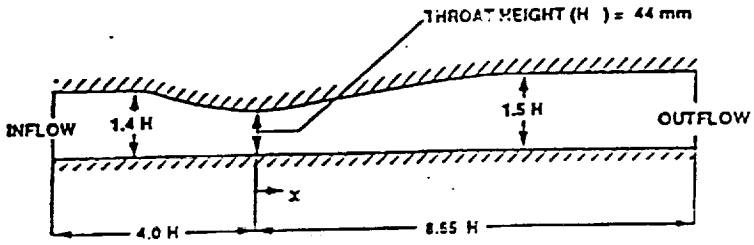

Figure 16. Illustration of the Sajben diffuser geometry.

Figure 17. Computational grid for the Sajben diffuser.

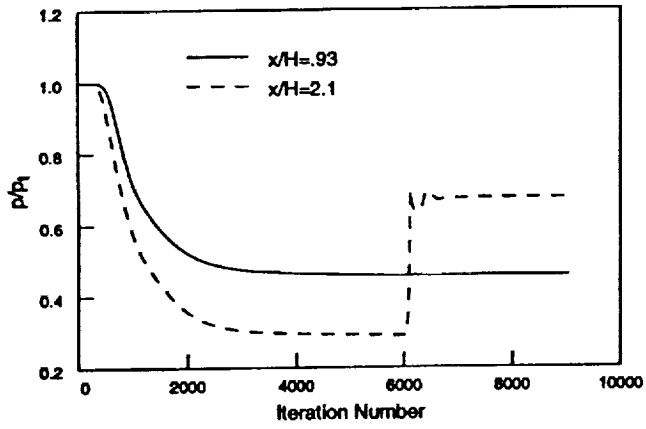

(a) MMLPG

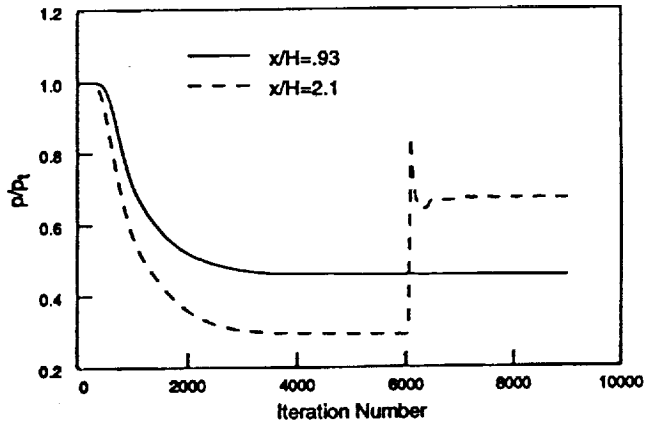

(b) BLM

Figure 18. Static pressure history at two locations on the top wall.

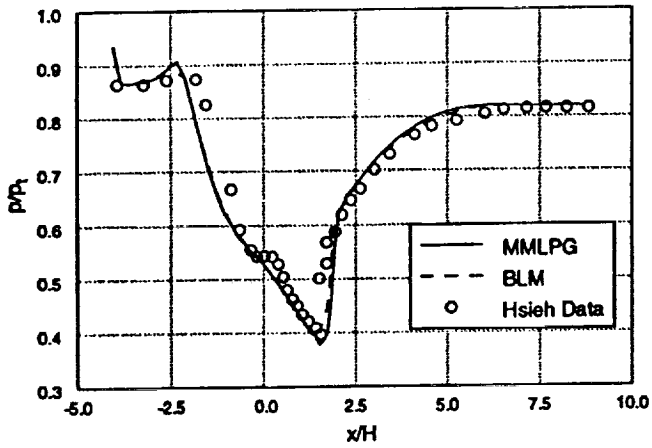

(a) Top wall

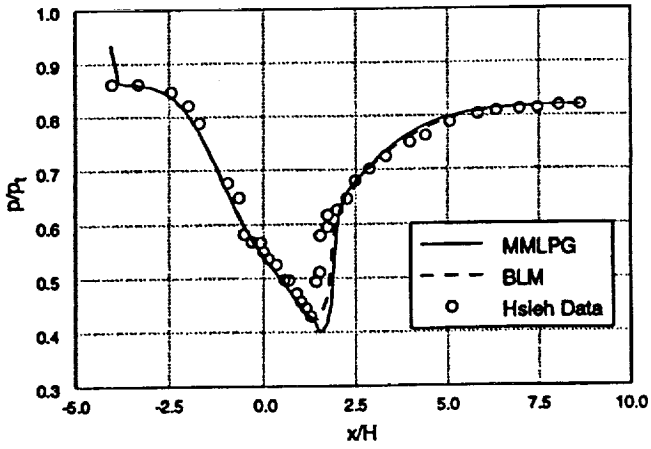

(b) Bottom wall

Figure 19. Static pressure on the Sajben diffuser top and bottom walls: weak shock case.

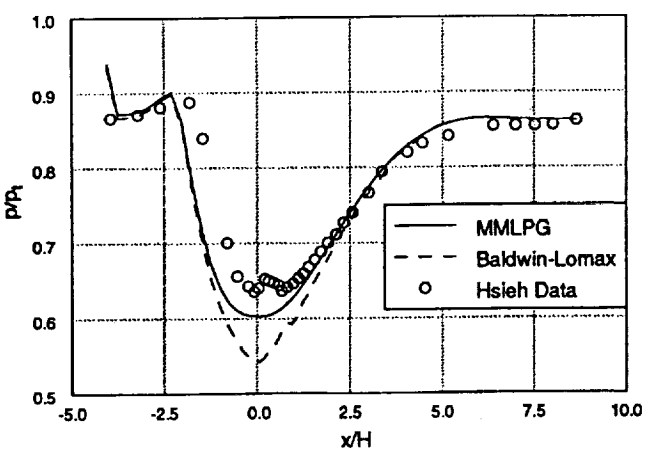

(a) Top wall

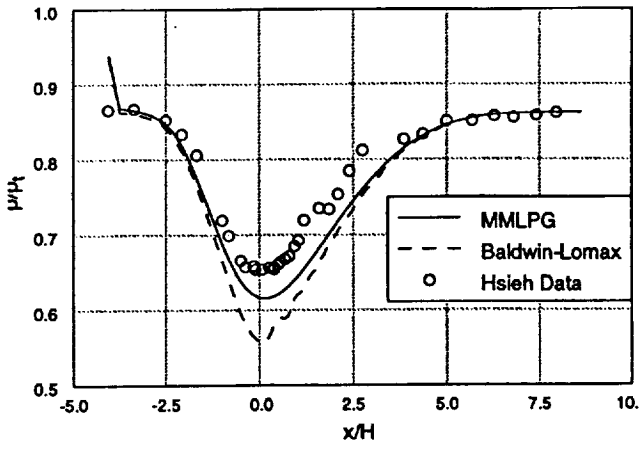

(b) Bottom wall

Figure 20. Static pressure on the Sajben diffuser top and bottom walls: no shock case.

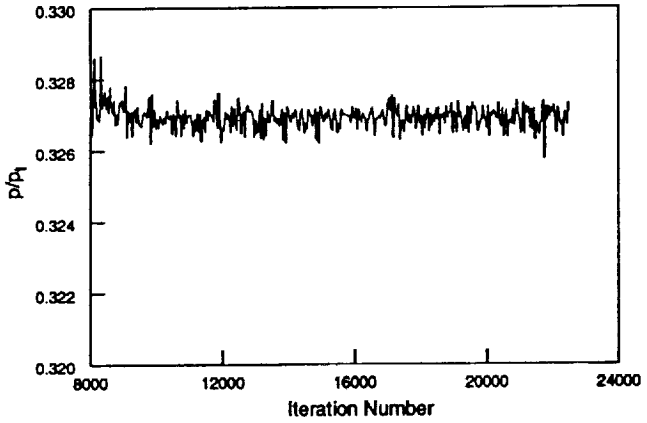

Figure 21. Shock static pressure on the Sajben diffuser top wall; strong shock case.

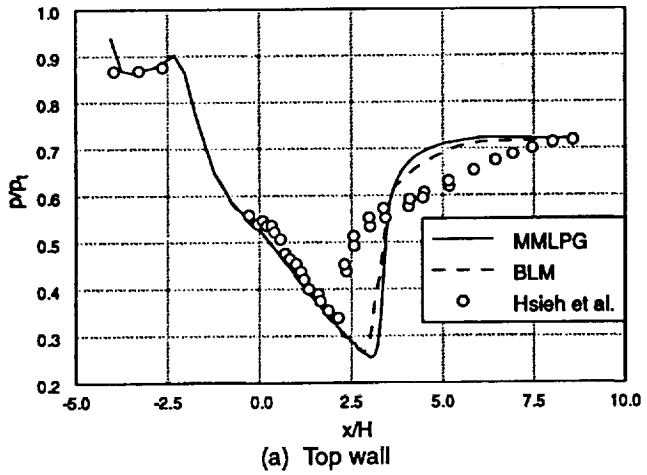

(a) Top wall

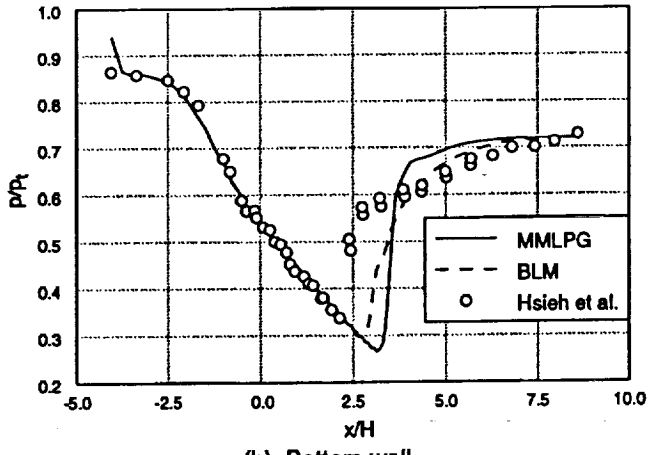

(b) Bottom wall

Figure 22. Static pressure on the Sajben diffuser top and bottom walls; strong shock case.

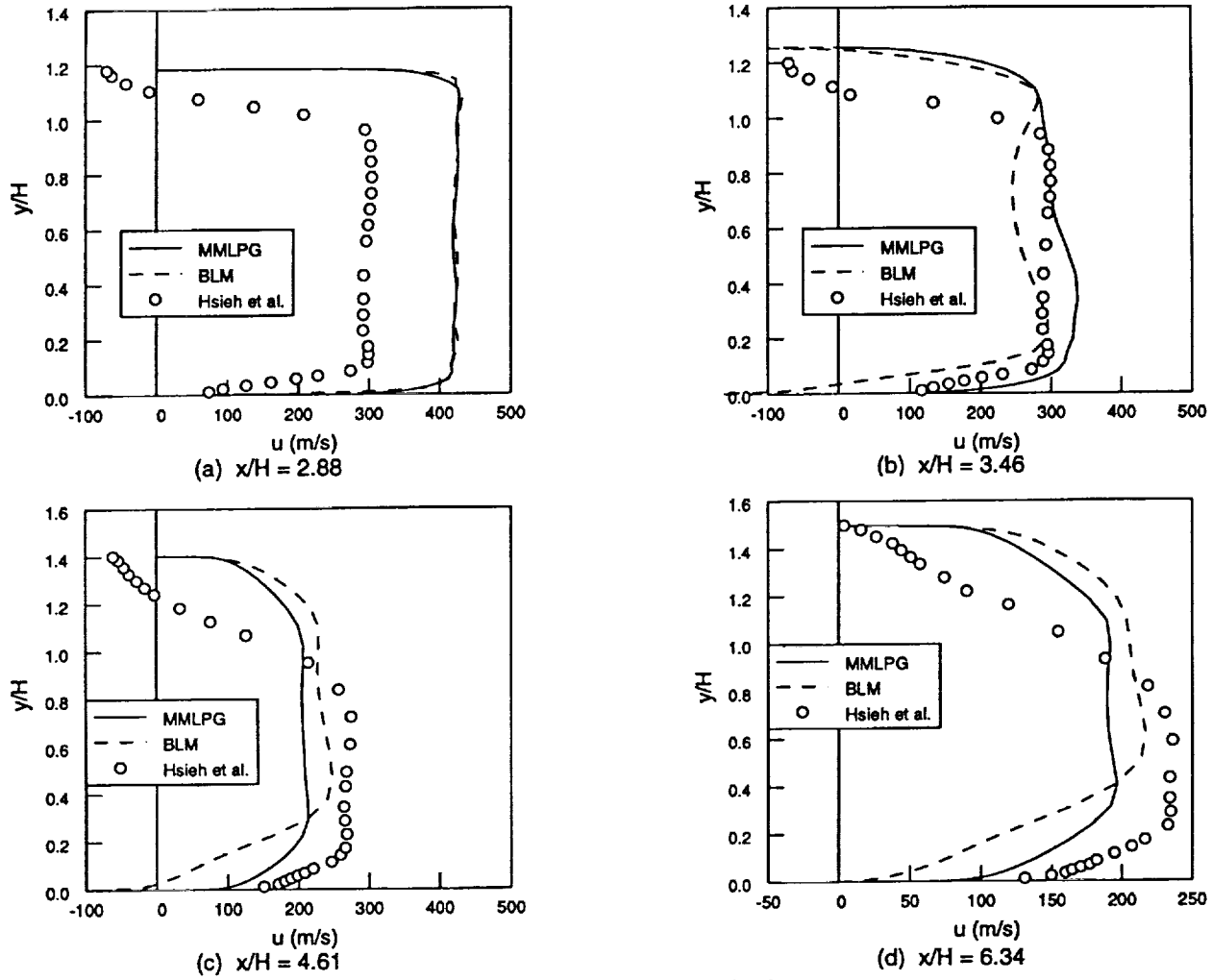

Figure 23. Velocity profiles for the strong shock case.

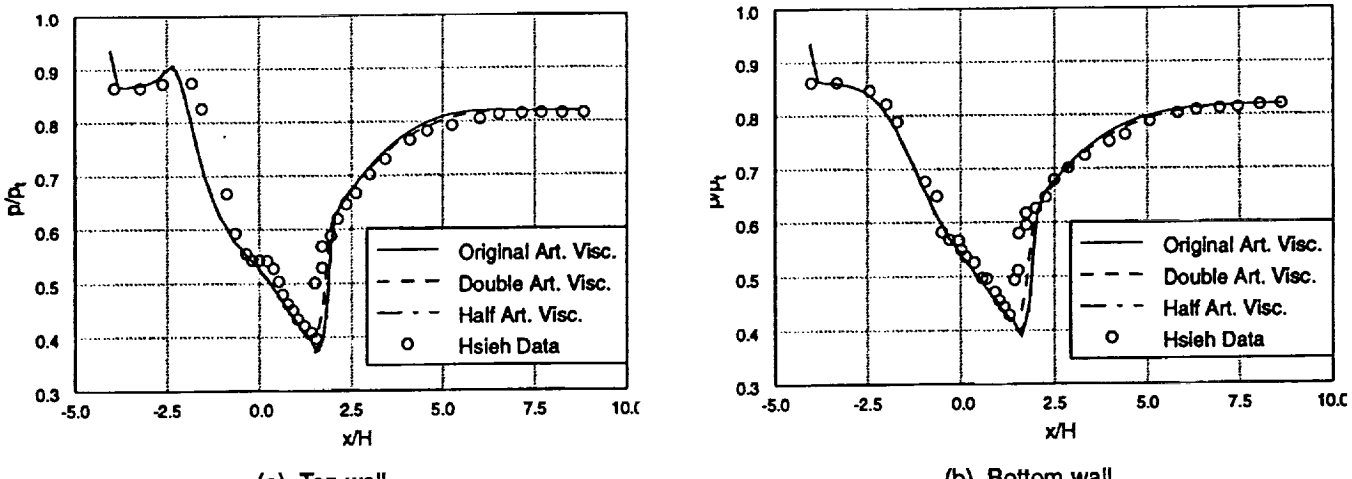

Figure 24. Static pressure, computed using MMLPG and three different amounts of artificial viscosity.

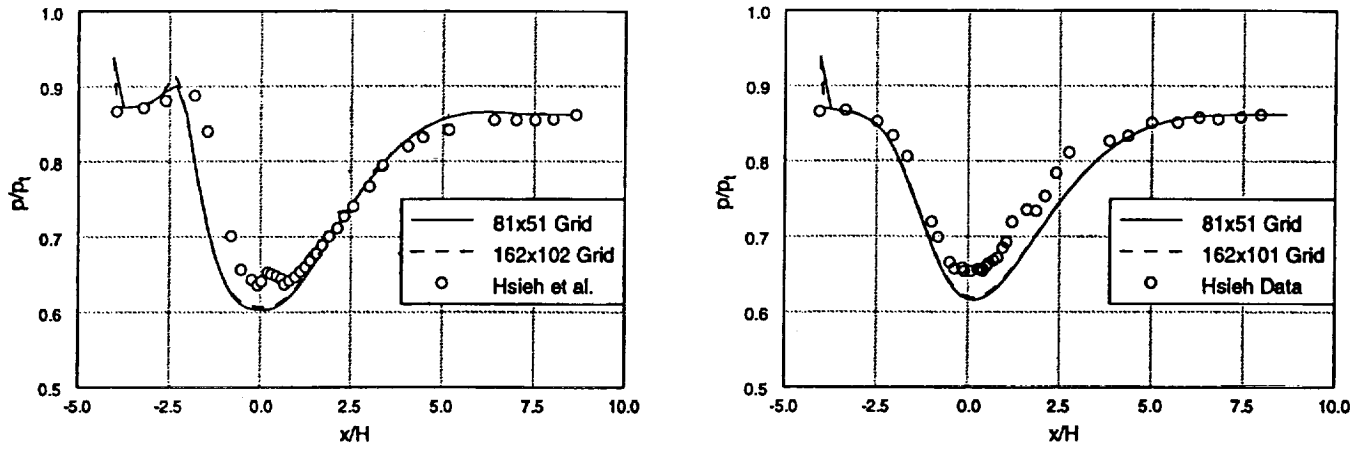

(a) Top wall

(b) Bottom wall

Figure 25. Static pressure computed using MMLPG and two different grids; no shock case.

REPORT DOCUMENTATION PAGE

Form Approved
OMB No. 0704-0188

1. AGENCY USE ONLY (Leave blank)	2. REPORT DATE	3. REPORT TYPE AND DATES COVERED
	November 1994	Technical Memorandum

4. TITLE AND SUBTITLE

A Modified Mixing Length Turbulence Model for Zero and Adverse Pressure Gradients

5. FUNDING NUMBERS

WU-505-62-52

6. AUTHOR(S)

J.M. Conley and B.P. Leonard

7. PERFORMING ORGANIZATION NAME(S) AND ADDRESS(ES)

National Aeronautics and Space Administration
Lewis Research Center
Cleveland, Ohio 44135-3191

8. PERFORMING ORGANIZATION REPORT NUMBER

E-9220

9. SPONSORING/MONITORING AGENCY NAME(S) AND ADDRESS(ES)

National Aeronautics and Space Administration
Washington, D.C. 20546-0001

10. SPONSORING/MONITORING AGENCY REPORT NUMBER

NASA TM-106772

11. SUPPLEMENTARY NOTES

Prepared for the 30th Joint Propulsion Conference cosponsored by AIAA, ASME, SAE, and ASEE, Indianapolis, Indiana, June 27-29, 1994 under the title "Modification of the MML Turbulence Model for Adverse Pressure Gradient Flows." J.M. Conley, NASA Lewis Research Center, and B.P. Leonard, The University of Akron, Akron, Ohio 44325. This material is a portion of NASA TM-106544 which was submitted by J.M. Conley as her Master's thesis. Responsible person, J.M. Conley, organization code 2660, (216) 433-2188.

12a. DISTRIBUTION/AVAILABILITY STATEMENT

Unclassified - Unlimited
Subject Category 34

12b. DISTRIBUTION CODE

13. ABSTRACT *(Maximum 200 words)*

The modified mixing length (MML) turbulence model was installed in the Proteus Navier-Stokes code, then modified to make it applicable to a wider range of flows typical of aerospace propulsion applications. The modifications are based on experimental data for three flat-plate flows having zero, mild adverse, and strong adverse pressure gradients. Three transonic diffuser test cases were run with the new version of the model in order to evaluate its performance. All results are compared with experimental data and show improvements over calculations made using the Baldwin-Lomax turbulence model, the standard algebraic model in Proteus.

14. SUBJECT TERMS

Navier-Stokes; Turbulent boundary layer; Two-dimensional flow; Mixing length flow theory; Pressure gradients; Flat plates; Computational fluid dynamics

15. NUMBER OF PAGES

23

16. PRICE CODE

A03

17. SECURITY CLASSIFICATION OF REPORT	18. SECURITY CLASSIFICATION OF THIS PAGE	19. SECURITY CLASSIFICATION OF ABSTRACT	20. LIMITATION OF ABSTRACT
Unclassified	Unclassified	Unclassified	